Chinese Chemical Letters 31 (2020) 2737–2741

Contents lists available at ScienceDirect

Chinese Chemical Letters

journal homepage: www.elsevier.com/locate/cclet

Communication

Oxygen vacancies on the BiOCl surface promoted photocatalytic complete NO oxidation *via* superoxide radicals

Jiazhen Liao[a], Kanglu Li[b,c], Hao Ma[a], Fan Dong[b], Xiaolan Zeng[a,*], Yanjuan Sun[b,*]

[a] College of Environment and Ecology, Chongqing University, Chongqing 400040, China
[b] Institute of Fundamental and Frontier Sciences, School of Resources and Environment, University of Electronic Science and Technology of China, Chengdu 611731, China
[c] College of Architecture and Environment, Sichuan University, Chengdu 610065, China

ARTICLE INFO

Article history:
Received 17 February 2020
Received in revised form 20 March 2020
Accepted 31 March 2020
Available online 27 April 2020

Keywords:
Oxygen vacancies
BiOCl
Visible light NO oxidation
Toxic byproduct
Reactive oxygen species

ABSTRACT

One of the core issues in the photocatalytic oxidation of nitric oxide is the effective conversion of NO into the final product (nitrate). More than just improving the visible light photocatalytic performance of BiOCl, we aim to inhibit the generation of toxic by-product NO_2 during this process. In this study, we demonstrate that the oxygen vacancies (OVs) modulate its surface photogenerated carrier transfer to inflect the NO conversion pathway by a facile mixed solvent method to induce OVs on the surface of BiOCl. The photocatalytic NO removal efficiency under visible light increased from 5.6% to 36.4%. In addition, the production rate of NO_2 is effectively controlled. The effects of OVs on the generation of reactive oxygen species, electronic transfer, optical properties, and photocatalytic NO oxidation are investigated by combining density functional theory (DFT) theoretical calculations, the *in situ* FTIR spectra and experimental characterization. The OVs on the surface of BiOCl speed the trapping and transfer of localized electrons to activate the O_2, producing $O_2^{\bullet-}$, which avoid NO_2 formation, resulting in complete oxidation of NO ($NO + O_2^{\bullet-} \rightarrow NO_3^-$). These findings can serve as the basis for controlling and blocking the generation of highly toxic intermediates through regulating the reactive species during the NO oxidation. It also can help us to understand the role of OV on the BiOCl surface and application of photocatalytic technology for safe air purification.

Nitric oxide (NO), even at a low concentration, is considered as a major contributor to ozone depletion, acid rain and photochemical smog, causing adverse effects on human health [1–4]. It is of a great challenge to achieved economical and efficient for NO removal at parts per billion (ppb) levels [5,6]. Semiconductor-based photocatalysis represents a competitive technology to treat NO air pollution [7–9]. However, the effective removal of dilute NO by photocatalytic technology in an environmentally friendly manner is also hampered by low removal efficiency and the generation of toxic by-products [10,11]. Toxic intermediate products, such as NO_2, are inevitably produced in the process of photocatalytic NO oxidation on typical photocatalysts [12,13]. For example, about 40% of NO is converted to more toxic NO_2 over g-C_3N_4-TiO_2 during photocatalytic NO oxidation [14,15]. Accordingly, the complete conversion of NO to nitrate is still a problem that researchers are committed to solving.

The three key steps that affect photocatalytic NO oxidation are as follows: (1) Light illumination, (2) separation and transfer of photogenerated electron-hole pairs, and (3) depletion [16–20]. By optimizing these three essential and complementary processes, the photocatalytic performance for pollutants oxidation can be improved [21–23]. Regrettably, in pursuit of high photocatalytic efficiency, the NO_2 generation has been ignored to some extent. The photogenerated hole and oxygen active species (ROS) directly participate in the photocatalytic NO oxidation. Analogous to electron-deficient molecular oxygen (O^-), photogenerated holes may cause partial oxidation of NO and produce NO_2 by-products ($NO + O^- \rightarrow NO_2$) [24,25]. Photogenerated electrons are captured by molecular oxygen to generate assorted ROS. Among them, superoxide radicals ($O_2^{\bullet-}$) is able to completely oxidize NO into final production ($NO + O_2^{\bullet-} \rightarrow NO_3^-$) [26,27]. Therefore, we expect to design an effective photocatalyst, and in unison, adjust the generated active species to suppress NO_2.

Bismuth oxychloride (BiOCl) is a typical ternary oxide material with low toxicity and high earth abundance [28–30]. It has attracted wide attention in the fields of photocatalytic pollutant

* Corresponding authors.
E-mail addresses: 276686704@qq.com (X. Zeng), syhsyj@163.com (Y. Sun).

https://doi.org/10.1016/j.cclet.2020.03.081
1001-8417/

control, water decomposition and energy conversion [31–34]. However, the photocatalytic efficiency of BiOCl remains unsatisfactory under visible light. Although it is proved that the introduction of oxygen vacancies (OVs) can enhance the photoreactivity of BiOCl [35–37], the intrinsic roles of OVs on the active species generation and inhibition of the toxic by-product need to be further investigated.

In this study, we demonstrate that OVs on the surface of BiOCl can much more readily activate oxygen to $O_2^{\bullet-}$ for NO complete oxidation. We also propose a possible mechanism to explain the formation of dominant active species $O_2^{\bullet-}$ and NO_2 inhibition over oxygen-defective BiOCl under visible light. The introduction of OVs effectively activates the oxygen molecules adsorbed on the surface of BiOCl. Under visible light, charge carriers generated by intraband excitation quickly combine with oxygen molecules to produce abundant $O_2^{\bullet-}$. The activated NO is directly oxidized to NO_3^- by $O_2^{\bullet-}$, which significantly inhibits the generation of NO_2.

Oxygen vacancies over surface of BiOCl are expected to influence $O_2^{\bullet-}$ generation, which can be tested by density functional theory (DFT) calculations (Detailed information on DFT is available in Supporting information). We simulated the adsorption of O_2 molecules (Figs. 1a and b) on the surfaces of BiOCl and BiOCl with oxygen vacancies (OV-BiOCl), respectively. The adsorption energy of OV-BiOCl (E_{ads} = −2.41 eV) is more negative than BiOCl (E_{ads} = −2.21 eV), which implies that oxygen molecules tend to be adsorbed on the surface of OV-BiOCl. Through the analysis of charge difference distribution, the charge transfer between O_2 and OV-BiOCl surface is more intense. Due to the weakening of the O—O coulomb interaction, the O—O bond length (1.44 Å) is increased significantly on OV-BiOCl. Thus, adsorbed O_2 molecules over OV-BiOCl are readily activated at the electron traps introduced by defects, and OVs transfer the collected electrons to O_2 for $O_2^{\bullet-}$ generation. Compared with BiOCl and OV-BiOCl (Figs. S1a and b in Supporting information), the almost constant O—H bond length can be considered as a slight activation of H_2O by OV, and the OV-BiOCl surface prefers to absorb O_2 (E_{ads} = −2.41 eV) over H_2O (E_{ads} = −1.99 eV). It makes superoxide radicals anticipated to be the dominant reactive oxygen species for the complete oxidation of nitric oxide.

Herein, pristine BiOCl (BCl) was synthesized *via* a hydrothermal method. The OV-BCl-x samples were prepared in the water/ethylene glycol (EG) mixed solvent. The synthesis procedures were the same as that of BCl, and OV-BCl-x samples were labeled as OV-BCl-1, OV-BCl-2 and OV-BCl-3 with the added ethylene glycol amount of 20, 40 and 60 mL, respectively. Detailed information on synthesis and characterization of the catalysts is available in Supporting information.

According to X-ray diffraction (XRD) spectra (Fig. 2a), all diffraction peaks of as-prepared BiOCl samples can be well indexed to the tetragonal phase of BiOCl (JCPDS No. 06-0249). OV-BCl-x gradually showed reduced diffraction peak intensity, indicating that the crystallinity decreased with the increase of the ethylene glycol content in the reaction solution. It is reported that the presence of ethylene glycol is beneficial to the formation of oxygen vacancies over the sample [35]. As shown in Bi 4f spectra of BCl and OV-BCl-3 samples (Fig. 2b), two additional peaks at 163.9 and 158.4 eV appeared in the Bi 4f spectra of OV-BCl-3, which originated from $Bi^{(3-x)+}$. The lower charge of Bi ions corresponds to the loss of oxygen atoms, which reveals the formation of oxygen vacancies on BiOCl [38]. The oxygen vacancy concentration of the prepared BiOCl sample can be observed in the electron paramagnetic resonance (EPR) spectra at low temperatures (Fig. 2c). Since the O atoms are removed from BiOCl, residual electrons are left on the OV sites. The EPR spectra of samples display a characteristic OV signal with a g factor of about 2.001 caused by these electron excess centers [39,40]. It can be deduced from the rising signal intensity that the residual electron concentration in OV-BCl-x has increased compared to BCl, which confirms the increase in OV concentration. These characterization results acknowledge that during the synthesis process, by changing the amount of ethylene glycol (EG) the concentration adjustment of OV on BiOCl is available, so that we can study the intrinsic role of OV in the visible light driven NO oxidation process. The SEM and TEM images of the samples are provided in Fig. S2 (Supporting information).

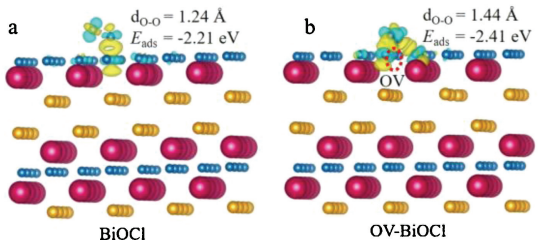

Fig. 1. Optimized O_2 adsorption and charge density difference of BiOCl (a) and OV-BiOCl (b). Electron accumulation is shown in blue and depletion in yellow. Blue, yellow and red spheres stand for O, Cl and Bi, respectively. The isosurfaces are set to 0.005 eV/Å^3.

The efficiency of photocatalysis is closely related to light absorption. When a semiconductor absorbs excitation energy that exceeds its bandgap energy, the electron transition on the valence band (VB) can be excited. On account of band gap width, BiOCl is virtually impossible to perform photocatalytic reaction under visible light. A key task is to perceive the change in optical absorption properties of OV-BCl-x caused by the introduction of defects. As shown by the UV–vis diffuse reflectance spectrum (DRS) (Fig. 3a), compared to BCl, the light absorption range of OV-BCl-x is greatly expanded. In addition to the absorption tail at about 420 nm, OV-BCl-3 also shows an absorption tail that decays exponentially in the ultraviolet and visible regions. To further explore the cause of enhanced light absorption, TDOS (total density of states) of BiOCl and OV-BiOCl were calculated by the hybrid DFT method, as shown in Fig. 3b. An obvious intermediate level is appeared under conduction band bottom of the OV-BiOCl, implying that the oxygen vacancies contribute to the formation of defect state, which could achieve electrons transition from intermediate level to conduction band (CB) under visible light irradiation [14,24]. The defect state is formed originating from the 6p orbitals of Bi element [19]. These results indicate that oxygen vacancies contribute to the formation of intermediate energy levels, which can achieve the transition of electrons from intermediate energy levels to the CB to reduce the formation of holes on VB, thereby avoiding NO_2 produced by hole oxidation [24,35]. Due to enhanced light absorption, added photo-generated electrons are produced on the catalyst surface.

The carrier concentration involved in the photocatalytic reaction affects the photocatalytic activity. Since the number of excited electrons is dominated by the separation efficiency, we use photoluminescence (PL) to examine the effect of OVs on the separation of photo-excited carriers. The PL spectra of BCl exhibit a strong fluorescence signal, while PL quenching is observed in the spectrum of the OV-BCl-x samples (Fig. 3c). We also monitored the carrier lifetime of the catalyst through nanosecond time-resolved fluorescence decay spectra (Fig. 3d). The charge carrier lifetime of OV-BCl-3 (1.187 ns) is longer than that of BCl (1.083 ns). Isolated carriers can participate in photocatalytic reactions before recombination, thereby increasing the number of effective charge carriers. When OV-BCl-3 absorbs visible light, the electrons are captured by the electron traps created by oxygen defects, forming local electron conduction, which is more conducive to the transfer of electrons to the surface adsorbed substance. These photoelectrochemical properties state clearly that the electron traps

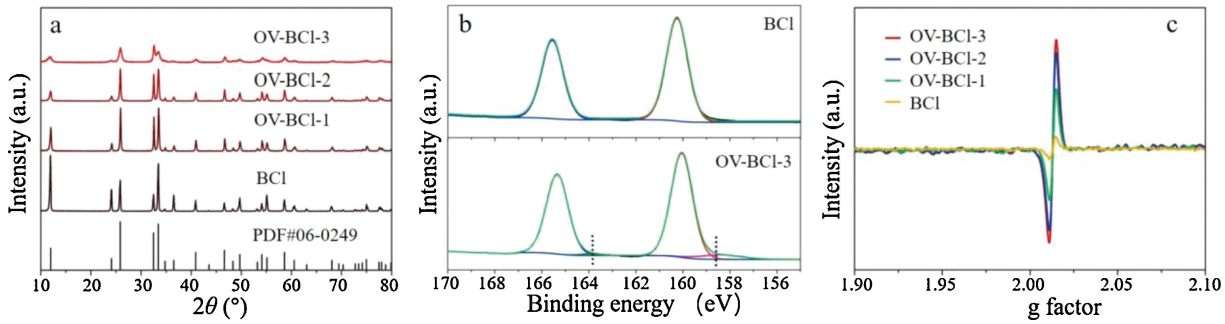

Fig. 2. (a) XRD spectra of BCl and OV-BCl-x. (b) XPS spectra (Bi 4f) of BCl and OV-BCl-3. (c) EPR spectra of BCl and OV-BCl-x.

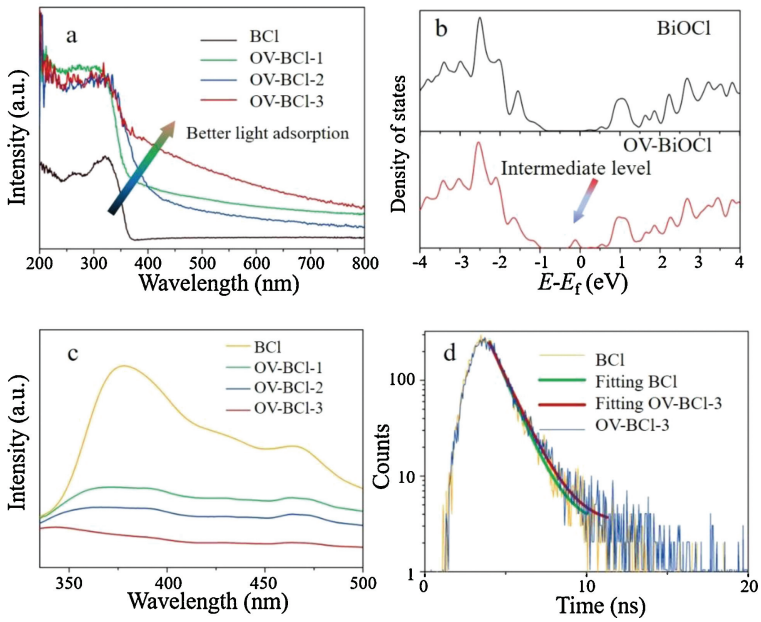

Fig. 3. UV–vis DRS spectra (a), density of states (DOS) of BiOCl and the introduction of oxygen vacancies OV-BiOCl (b). The Fermi level is set to 0 eV. PL spectra (c), Nanosecond-level time-resolved fluorescence spectra surveyed at room temperature for BCl and OV-BCl-3 (d).

formed at the O defect sites effectively inhibit the recombination and promote the rapid transfer of photo-excited charge carriers, thereby facilitating photocatalytic reactions. Photocatalytic visible light absorption, charge transfer, and reactant activation are three interrelated steps, and changes in each step will affect the photocatalytic activity. Excellent light absorption is the first step in the conversion of light energy by photocatalysts, and is able to generate more electron-hole pairs under light excitation. The charge transfer determines the number of effective electron-holes that can participate in the reaction. The reactants activation can improve the utilization efficiency of electrons and holes, and make the reactants readily converted.

Encouraged by the calculation results, $O_2^{\bullet-}$ was detected by the 5,5-dimethyl-1-pyrroline *N*-oxide (DMPO) spin-trapping electron spin resonance (ESR). The detected DMPO $O_2^{\bullet-}$ signal (Fig. 4a) increases with the increase of the oxygen vacancy concentration of BiOCl, proving that the ameliorative adsorption of O_2 molecules and more intense local electron transfer enable O_2 molecules to be activated to generate $O_2^{\bullet-}$ radicals. The band position of BiOCl (E_{VB} = 3.43 eV, E_{CB} = 0.23 eV) can be calculated by empirical formula

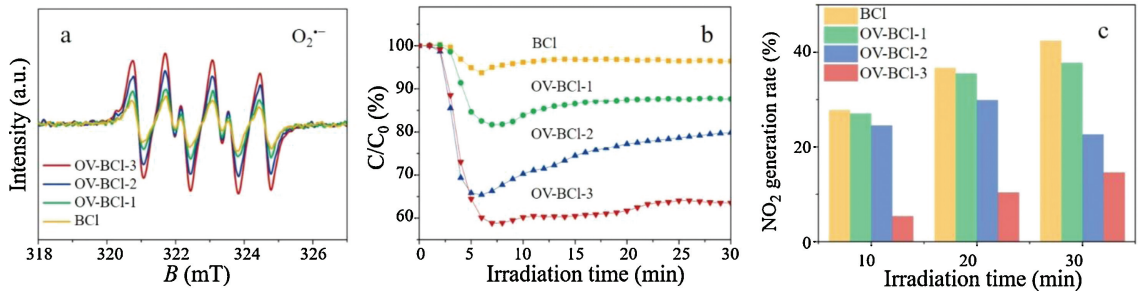

Fig. 4. DMPO spin-trapping ESR spectra in methanol dispersion for $O_2^{\bullet-}$, which are carried out in visible light irradiation for 15 min (a), Photocatalytic activity of BiOCl samples for the removal of NO (b) and the NO_2 generation rate (c).

$E_{VB} = X - E^e + 0.5E_g$. It seems that the CB potential of BiOCl (0.23 eV) is less negative than the redox potential of $O_2/O_2^{\bullet-}$ (−0.33 eV). Notably, the CB has a certain breadth, so electrons can be photoexcited to higher levels of the CB. As a result, superoxide radicals can still be generated as evidenced by the ESR (Fig. 4a). In addition, since the presence of $^{\bullet}OH$ depends on the generation path of $O_2^{\bullet-} \rightarrow H_2O_2 \rightarrow {}^{\bullet}OH$, a characteristic signal of DMPO-$^{\bullet}OH$ also appears (Fig. S3 in Supporting information). Abundant ROS were deemed to be essential to promote rapid photocatalytic oxidation of NO (Reactions 1–4).

$$NO + O_2^{\bullet-} \rightarrow NO_3^- \quad (1)$$

$$NO + {}^{\bullet}OH \rightarrow NO^+ + OH^- \quad (2)$$

$$NO^+ + 2OH^- \rightarrow H_2O + NO_2^- \quad (3)$$

$$NO + 2{}^{\bullet}OH + 2OH^- \rightarrow 2H_2O + NO_3^- \quad (4)$$

To verify the relationship between OV and NO complete oxidation, we occupied the as-prepared samples to remove NO (diluted about 500 ppb) in a continuous flow reactor under visible light illumination. As shown in Fig. 4b, the BCl sample can barely remove NO efficiently under visible light. As for BCl-x, we observe that the NO degradation rate increases with increasing OV concentration, while the NO_2 generation rate gradually decreases. BCl-3 reaches 36.5% NO removal efficiency in 30 min. Concurrent with the rise in removal rate of NO is the lower generated rate of NO_2. As expected, the generation rate of NO_2 has declined significantly (Fig. 4c), which indicates that most NO is directly oxidized to nitrate. During the photocatalytic reaction, the generated nitrate products adhered to the catalyst surface and occupied the active site of the catalyst, resulting in a slight decrease in the NO removal rate (Fig. 4b). Surface contaminants of photocatalysts can be removed by simple flushing. Due to the introduction of vacancies on BiOCl, numerous superoxide radicals are generated and OV-containing samples are excellent at degrading other contaminants. The removal efficiency of tetracycline hydrochloric acid in wastewater on BCl-x are also significantly improved (Fig. S4 in Supporting information).

To further study the photocatalytic reaction as to superoxide radical promotes the complete oxidation of NO into nitrate, *in situ* DRIFT measurement was used for dynamic monitoring research (Scheme S1 in Supporting information). Table S1 (Supporting information) lists the assignment of the observed bands. Fig. 5a shows the time evolution of the IR spectra during the NO adsorption process over BCl-3. The stretching vibration of 1091 cm^{-1} is derived from the adsorbed NO on BCl-3 [24]. The absorption bands of NO^- (1174 cm^{-1}) [41] and nitro surface species (1280 cm^{-1}) [44] are observed. The species responsible for the band (1280 cm^{-1}) interact with NO to form nitrate species (1212 cm^{-1}) [44,45]. The researchers report that some substances responsible for this band (1280 cm^{-1}) further react to form nitrates during vacuum evacuation at room temperature, while others are thermally stable [44,46]. The DFT calculation reveals that the N–O bond length is elongated from 1.17 Å to 1.19 Å from defect-free to defective (Figs. S1b and d in Supporting Information). It is proved that oxygen vacancies on the surface of BiOCl facilitate the adsorption and activation of NO. Activated NO can be rapidly transformed into NO_3^- by ROS. As shown in Fig. 5b, the final products (nitrates) of photocatalytic NO oxidation on BCl-3 are increased substantially due to oxidation of adsorbed NO under visible light. A retrorse peak corresponding to NO (1057 cm^{-1}) is detected [25,41]. The O—O stretching mode of $O_2^{\bullet-}$ species (1003 cm^{-1}) are found [24], while NO_3^- (1274, 1329, 1480 cm^{-1}) has gradually accumulated [42–44]. Electron traps formed at the oxygen defective site promote stronger electron exchange between the catalyst surface and the reactants, leading to the activation of NO and the generation of $O_2^{\bullet-}$.

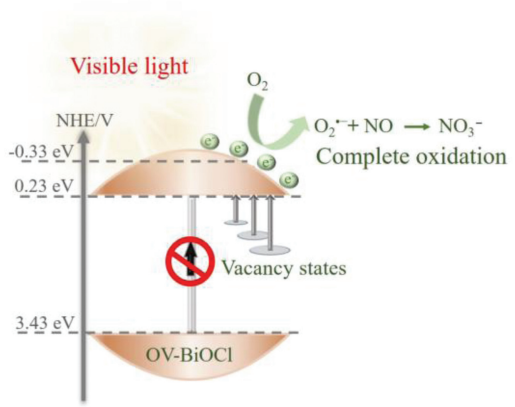

Fig. 6. The illustration of the roles of oxygen vacancy in photocatalytic NO oxidation.

Further, the photocatalytic oxidation of NO to nitrate is directly related to $O_2^{\bullet-}$ generated by intraband excitation of BiOCl, while holes remaining on the defective level present low oxidative ability, avoiding partial oxidation of NO ($NO + O^- \rightarrow NO_2$) (Fig. 6). Generally, semiconductors are excited to generate electron-hole pairs, and the holes can directly participate in the oxidation of the reactants. However, in the process of NO oxidation, holes are similar to electron-deficient molecular oxygen, which easily generate NO_2, leading to augmentation of toxic by-product. Activated NO is preferentially converted into NO_3^- by $O_2^{\bullet-}$ radicals, reducing the generation of toxic by-products. Therefore, the introduction of oxygen defects over BiOCl expands the range of light absorption,

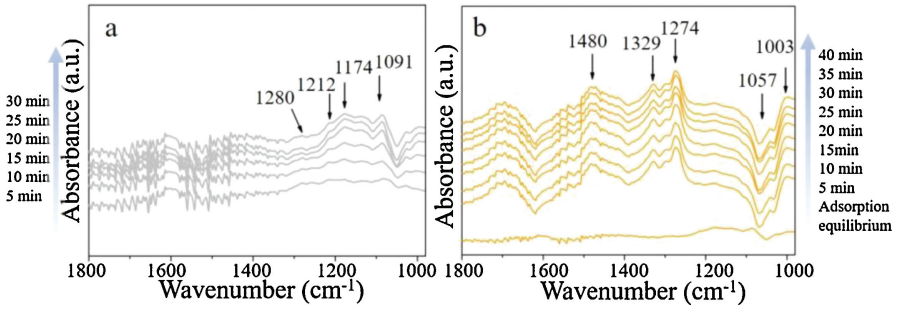

Fig. 5. *In situ* DRIFTS spectra on BCl-3 during NO adsorption process (a) and photocatalytic NO oxidation process (b).

accelerates electron transfer to form superoxide radicals, and ultimately promotes the complete oxidation of NO to NO_3^-.

In conclusion, we have demonstrated that introduced oxygen vacancies on the surface of BiOCl can readily activate molecular oxygen for $O_2^{\bullet-}$ generation for NO removal under visible light. Combining DFT calculation and experimental methods, the conversion pathway of photocatalytic NO complete oxidation and mechanism of toxic intermediate (NO_2) inhibition are revealed. The introduction of oxygen vacancies advances the local conduction of charge carriers on the surface of BiOCl, making O_2 the dominant oxide species to directly react with activated NO, and NO is rapidly oxidized to the final product with significant suppression of NO_2 production. These findings gain deep insight into the relationship between OVs and active species, and shed light on the inhibition of NO_2 formation during effective photocatalytic NO removal for efficient and safe air purification.

Declaration of competing interest

The authors declare that they have no known competing financial interests or personal relationships that could have appeared to influence the work reported in this paper.

Acknowledgments

This work was supported by the National Natural Science Foundation of China (Nos. 21822601, 21777011 and 21501016), and the Plan for "National Youth Talents" of the Organization Department of the Central Committee. The authors also acknowledge the AM-HPC in Suzhou, China for computational support.

Appendix A. Supplementary data

Supplementary material related to this article can be found, in the online version, at doi:https://doi.org/10.1016/j.cclet.2020.03.081.

References

[1] W. Cui, J. Li, F. Dong, et al., Environ. Sci. Technol. 51 (2017) 10746–10753.
[2] K. Li, W. Cui, J. Li, et al., Chem. Eng. J. 378 (2019) 122184.
[3] P. Chen, H. Liu, Y. Sun, et al., Appl. Catal. B: Environ. 264 (2020) 118545.
[4] B. Lei, W. Cui, J. Sheng, et al., Sci. Bull. 65 (2020) 467–476.
[5] Z. Ai, W. Ho, S. Lee, L. Zhang, Environ. Sci. Technol. 43 (2009) 4143–4150.
[6] R. Chen, H. Wang, H. Wu, et al., Chin. J. Catal. 41 (2020) 710–718.
[7] J. Yi, J. Liao, K. Xia, et al., Chem. Eng. J. 370 (2019) 944–951.
[8] Y. Zou, Y. Xie, S. Yu, et al., Appl. Surf. Sci. 496 (2019) 143630.
[9] J. Jin, J. Chen, H. Wang, P. Hu, Chin. Chem. Lett. 30 (2019) 618–623.
[10] W. Cui, J. Li, Y. Sun, et al., Appl. Catal. B: Environ. 237 (2018) 938–946.
[11] X. Li, W. Zhang, J. Li, et al., Appl. Catal. B: Environ. 241 (2019) 187–195.
[12] W. Wang, G. McCool, N. Kapur, et al., Science 337 (2012) 832–835.
[13] J. Li, W. Cui, Y. Sun, et al., J. Mater. Chem. A 5 (2017) 9358–9364.
[14] H. Shang, M. Li, H. Li, et al., Environ. Sci. Technol. 53 (2019) 6444–6453.
[15] J. Ma, C. Wang, H. He, Appl. Catal. B: Environ. 184 (2016) 28–34.
[16] L. Zhang, C. Yang, K. Lv, et al., Chin. J. Catal. 40 (2019) 755–764.
[17] J. Liao, W. Cui, J. Li, et al., Chem. Eng. J. 379 (2020) 122282.
[18] X. Li, W. Zhang, J. Li, et al., Appl. Catal. B: Environ. 241 (2019) 187–195.
[19] M. Xiao, Z. Wang, M. Lyu, et al., Adv. Mater. 31 (2019) 1801369.
[20] D. Yuan, M. Sun, S. Tang, et al., Chin. Chem. Lett. 31 (2020) 547–550.
[21] H. Wang, W. Zhang, X. Li, et al., Appl. Catal. B: Environ. 225 (2018) 218–227.
[22] X. Dong, W. Cui, H. Wang, et al., Sci. Bull. 64 (2019) 669–678.
[23] Q. Shen, L. Zhang, N. Sun, et al., Chem. Eng. J. 322 (2017) 46–55.
[24] H. Li, H. Shang, X. Cao, et al., Environ. Sci. Technol. 52 (2018) 8659–8665.
[25] C. Yuan, W. Cui, Y. Sun, et al., Chin. Chem. Lett. 31 (2020) 751–754.
[26] J. Lasek, Y. Yu, J.C. Wu, J. Photochem. Photobio. C Photochem. Rev. 14 (2013) 29–52.
[27] F. Dong, Z. Wang, Y. Li, W. Ho, S.C. Lee, Environ. Sci. Technol. 48 (2014) 10345–10353.
[28] R. Jiang, G. Lu, Z. Yan, et al., Chem. Eng. J. 374 (2019) 79–90.
[29] S. Li, J. Chen, Y. Liu, K. Xu, J. Liu, J. Alloys. Compd. 781 (2019) 582–588.
[30] Z. Zhao, Y. Cao, F. Dong, et al., Nanoscale 11 (2019) 6360–6367.
[31] W. Ouyang, F. Teng, X. Fang, Adv. Funct. Mater. 28 (2018) 1707178.
[32] A. Kumar, A. Kumar, G. Sharma, et al., Chem. Eng. J. 334 (2018) 462–478.
[33] H. Chen, X. Wang, W. Bi, Y. Wu, W. Dong, J. Colloid Interface Sci. 502 (2017) 89–99.
[34] H. Hao, Y. Xu, P. Liu, G. Zhang, Chin. Chem. Lett. 26 (2015) 133–136.
[35] H. Li, J. Shi, K. Zhao, L. Zhang, Nanoscale 6 (2014) 14168–14173.
[36] L. Hao, Q. Feng, Z. Yang, et al., J. Am. Chem. Soc. 139 (2017) 3513–3521.
[37] H. Liu, P. Chen, X. Yuan, et al., Chin. J. Catal. 40 (2019) 620–630.
[38] J. Jiang, L. Zhang, H. Li, W. He, J.J. Yin, Nanoscale 5 (2013) 10573–10581.
[39] S.N. Steinmann, S.T. Melissen, T. Le Bahers, P. Sautet, J. Mater. Chem. A 5 (2017) 5115–5122.
[40] W. Cui, H. Wang, J. Li, et al., Sci. Bull. 64 (2019) 669–678.
[41] K. Hadjiivanov, Catal. Rev. 42 (2000) 71–144.
[42] K. Hadjiivanov, V. Avreyska, A. Dimitar Klissurski, T. Marinova, Langmuir 18 (2012) 1619–1625.
[43] L. Jaan, J.R. Ohlsen, Chem 27 (2007) 465–513.
[44] M.A. Debeila, N.J. Coville, M.S. Scurrell, G.R. Hearne, Appl. Catal. A: Gen. 291 (2005) 98–115.
[45] Y. Zhou, Z. Zhao, F. Wang, et al., J. Hazard. Mater. 307 (2016) 163–172.
[46] K. Hadjiivanov, H. Knözinger, Phys. Chem. Chem. Phys. 2 (2000) 2803–2806.